Landslides (2017) 14:2129–2146
DOI 10.1007/s10346-017-0907-7
Received: 17 July 2017
Accepted: 2 October 2017
Published online: 10 October 2017

Xuanmei Fan · Qiang Xu · Gianvito Scaringi · Lanxin Dai · Weile Li · Xiujun Dong · Xing Zhu · Xiangjun Pei · Keren Dai · Hans-Balder Havenith

Failure mechanism and kinematics of the deadly June 24th 2017 Xinmo landslide, Maoxian, Sichuan, China

Abstract At 5:38 am on the 24th June, 2017, a catastrophic rock avalanche destroyed the whole village of Xinmo, in Maoxian County, Sichuan Province, China. About 4.3 million m^3 of rock detached from the crest of the mountain, gained momentum along a steep hillslope, entrained a large amount of pre-existing deposits, and hit the village at a velocity of 250km/h. The impact produced a seismic shaking of ML=2.3 magnitude. The sliding mass dammed the Songping gully with an accumulation body of 13 million m^3. The avalanche buried 64 houses; 10 people were killed and 73 were reported missing. The event raised great concerns both in China and worldwide. Extensive field investigation, satellite remote sensing, UAV aerial photography, and seismic analysis allowed to identify the main kinematic features, the dynamic process, and the triggering mechanism of the event. With the aid of ground-based synthetic aperture radar monitoring, the hazard deriving from potential further instabilities in the source area has been assessed. The preliminary results suggest that the landslide was triggered by the failure of a rock mass, which had been already weakened by the M_s 7.5 Diexi earthquake in 1933. Several major earthquakes since then, and the long-term effect of gravity and rainfall, contributed to the mass failure. The high elevation, slope angle, and vegetation cover in the source area hinder geological field investigation and make hazard assessment difficult. Nonetheless, monitoring and prevention of similar collapses in mountainous areas must be carried out to protect human lives and infrastructures. To this aim, the integrated use of modern high-precision observation technologies is strongly encouraged.

Keywords Rock avalanche · Landslide · Diexi earthquake · Failure mechanism · UAV and InSAR

Introduction

At about 5:38 am local time on Saturday, 24th June, 2017 (21:38 UTC of June 23rd), a massive rock avalanche destroyed the village of Xinmo in Maoxian County, Sichuan Province, in southwestern China (N 32° 04′ 47″, E 103° 39′ 46″). The landslide buried 64 houses and killed 10 people. Further 73 people were reported missing. The sliding mass blocked 1.0 km of river and damaged 1.5 km of road. It was one of the most catastrophic landslide events in the recent years in China and it attracted widespread attention from both the public and the academic community in China and abroad.

The source mass detached from the top of the mountain ridge at an average elevation of 3431 m a.s.l. and slid until the Songping river, which flows at 2280 m. The mass covered a distance of more than 2600 m, with a height relief of almost 1200 m, and formed an accumulation body, about 1200 m wide along the river, 500 m long and more than 10 m thick. The landslide event can be regarded as a rock avalanche following the updated Varnes classification (Hungr et al. 2014). It featured a large rockslide in the source area which evolved in an extremely rapid (Cruden and Varnes 1996) flow-like movement of fragmented rock that mobilized and entrained a large amount of debris of an old landslide deposit along its run.

The landslide occurred in a geologically fragile and tectonically active region with frequent strong seismic records. Three major earthquakes occurred in the past hundred years: the 1933 Diexi earthquake (M_s 7.5), the 1976 Songpan-Pingwu earthquake (M_s 7.2), and the great Wenchuan earthquake (M_w 7.9) (Huang et al. 2009; Wang et al. 2011). The 1933 event was the most destructive one in the region and induced a large number of landslides and landslide dams (Chai et al. 1995; Wang et al. 2008). Three of them (Dahaizi, Xiaohaizi, and Diexi dams, see Fig. 1) reached a height of 160 m above the Minjiang river. Forty-five days after the earthquake, the three dammed lakes merged and subsequently emptied during a giant dam-break flood that rushed downstream for a distance of 250 km, killing more than 2500 people (Chai et al. 1995). The dam-break event accounts for over one third of fatalities related to the Diexi earthquake. Ling (2015) reconstructed the Diexi landslide dam profile and estimated the peak discharge of the dam-breach outburst flood to be in the order of 20,000 m^3/s, which was probably the largest flood in the recent history in China. Several smaller barrier lakes induced by the Diexi earthquake also formed along the Songping river, which is a first-order tributary of the Minjiang river (Fig. 1). The remote sensing images show clearly that the Xinmo village was built on the deposits of an old landslide induced by the 1933 earthquake. This landslide dammed the Songping river, forming the Bailazhai barrier lake. The recent Xinmo landslide occurred on the very same site.

Immediately after the 24th June landslide event, the State Council launched on-site emergency rescue and disaster relief operations. Within 2 h from the disaster, our research team based at the State Key Laboratory of Geohazard Prevention and Geoenvironment Protection (SKLGP) in Chengdu, together with the emergency response team of Sichuan Land and Resources Department, reached the site with advanced equipment, including an unmanned aerial vehicle (UAV) and a ground-based synthetic aperture radar (GBSAR). The corresponding author of this paper (prof. Qiang Xu), as the leader of the on-site expert board, was directly involved in the investigation and analysis of the causes of the landslide and in the prevention of secondary disasters, and has collected valuable first-hand data.

Since after the event, the following research questions have become hot issues under discussion:

(1) How did, and to what extent, the previous earthquakes contribute to the current landslide event?
(2) Did the source mass exhibit any precursors before sliding and what was its deformation history?

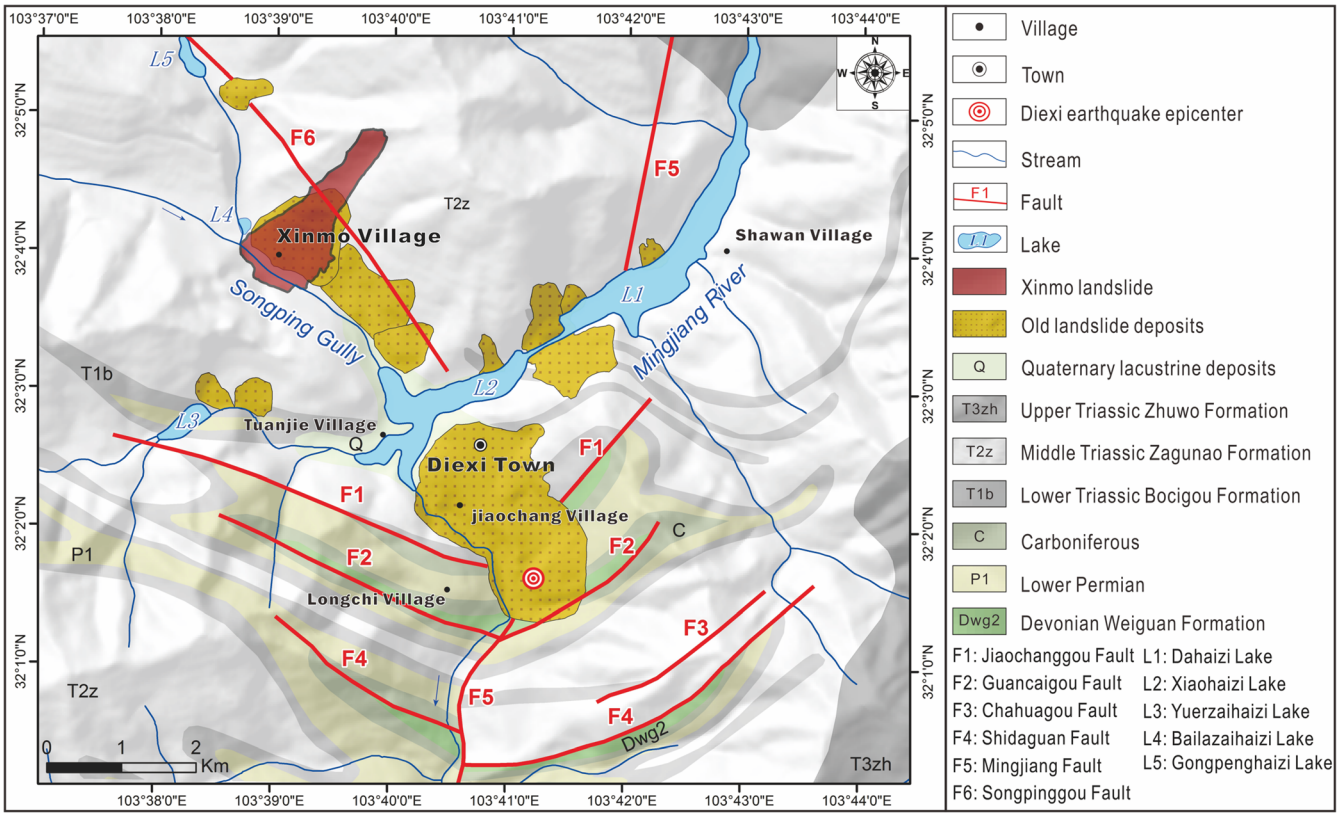

Fig. 1 Geological map of the study area indicating the location of the Xinmo landslide, old landslide deposits, barrier lakes and active faults

(3) Will further failures occur on the same mountain crest, and will any new landslides be triggered during the rainfall season in this region?
(4) Is it possible to perform early recognition and warning of such kind of landslides, originating in inaccessible, high-elevation and steep mountain slopes with dense vegetation, and, if so, how?

To the best of the knowledge we acquired so far, this paper discusses possible answers and views to the above questions. During the emergency rescue, a UAV was flown to obtain high-resolution images and produce a digital surface model (DSM). Together with pre-sliding multi-temporal remote sensing images, digital elevation models (DEM) and data from interferometric synthetic aperture radar (InSAR), the deformation history and the geomorphological features of the landslide have been identified and analyzed. The volume of the source material and the deposition mass was calculated by comparing pre- and post-sliding DEMs. Landslide-generated seismogram traces at the nearby Maoxian broadband seismic station have been used to identify the initiation and travelling times of the landslide and get an independent estimation of the displaced mass. The first post-sliding monitoring data have been analyzed to assess the potential residual hazard in the area and are presented in this work.

Geological settings

The landslide developed at the top of a sharp ridge line, at an average elevation of 3431 m a.s.l, on the left bank of the Songping river, a first-order tributary of the Minjiang river. The site is characterized by rugged alpine terrain due to strong tectonic erosion. The microclimate is mainly influenced by the monsoon climate of the East Tibetan Plateau, with an average annual temperature of 11.0 °C, an average annual precipitation of 716.5 mm, and a maximum recorded daily rainfall of 104.2 mm (Wang et al. 2008).

The strata outcropping in the area belong to the Weiguanqun formation of the Devonian (Dwg_2), Carboniferous (C) and Lower Permian (P_1) periods, and to the Bocigou (T_1b) and the Zagunao (T_2z) formations of the Triassic (Fig. 1). They mainly consist of metamorphic sandstone, marbleized limestone and phyllite. The Xinmo landslide developed within the Zagunao formation (T_2z), which at this location consists of metamorphic sandstone intercalated with slate. The attitude of the strata is N 80° W / SW ∠ 47°. The slope is a typical bedding-controlled slope, as the dip of the strata and the aspect of the slope are practically coincident (Bromhead 2013). The deposit of an old landslide triggered by the Diexi earthquake in 1933 (Li et al. 1986) lies at the slope foot just below the source area.

The landslide area lies atop the Jiaochang arcuate structure within the Songpan-Ganzi fold-belt (Deng et al. 2013). In the area, four arcuate faults are identified (Fig. 1). Moving from Jiaochang village southwards, they are named Jiaochanggou Fault (F_1), Guancaigou Fault (F_2), Chahuagou Fault (F_3) and Shidaguan Fault (F_4). A North-South distributing fault (the Minjiang Fault, F_5) crosses the arcs in the middle, while a North-West trending fault (the Songpinggou Fault, F_6) crosses

them slantwise. This latter fault develops nearly along the Songping river, originating from Moshi village, running in east-south direction towards Songping Town, Baila village and ending at Guanyinya near Jiaochang village. The fault intersects the deposits of the old landslide as well, and it played a clear triggering and controlling effect on the development of geological hazards in the area (Wang et al. 2008).

This fault system belongs to a broader area of high tectonic activity—the North-South seismic zone (e.g., Li et al. 2016)—within the Minshan block, of which the Longmenshan structural belt constitutes the south boundary and the Songpinggou fault is part of its west boundary (Xu et al. 2009; Wang et al. 2011). The area has experienced the 1933 M_s 7.5 Diexi earthquake, the 1976 M_s 7.2 Songpan-Pingwu earthquake and the 2008 M_w 7.9 great Wenchuan earthquake. The epicenter of the 1933 earthquake was very close to the towns of Jiaochang and Diexi, where the seismic intensity reached Level X (Chai et al. 1995) in the Chinese Seismic Intensity Scale (Lee 1954 and subsequent modifications) and numerous large-scale rockfalls and landslides were triggered. The mass movements blocked the Minjiang river and the Songping river in several locations, forming over 10 string-distributed dammed lakes of different scales (Wang et al. 2008), as shown in Fig. 1. The local seismic intensity of the 1976 earthquake reached Level VI in this area (Jones et al. 1984), while that of the 2008 Wenchuan earthquake reached Level VII and did not trigger large-scale geological hazards (Huang and Li 2009).

Data and methods

After the Xinmo landslide, relevant organizations and scholars actively collaborated to provide valuable information for this study. By collecting data from multiple sources and analyzing them with various techniques, this work probably contains the first complete overview of the landslide event with respect to its geoenvironment conditions, deformation history, failure mechanism, kinematic characteristics and secondary hazards assessment. Table 1 and Fig. 2 summarize the data and the general methodology followed in the study. Details are as follows:

(1) Visual interpretation based on multi-temporal satellite images

In order to investigate the deformation history of the Xinmo landslide, three scenes of remote-sensing images prior to the landslide were collected and analyzed through visual interpretation (see "Deformation history of the landslide" section). The earliest image dates August 18th, 2003 from Google Earth, while the two most recent images were obtained by the Chinese Gaofen-2 satellite on February 9th, 2016 and on April 8th, 2017. The ground resolution of the images (0.8 m) is sufficient for the identification of macroscopic deformation indicators, such as macro-cracks and talus (e.g., Zhang et al. 2013; Tian et al. 2017).

To acquire post-sliding data, our research team relied on the use of a F1000 UAV (produced by Feima Robotics, Ltd) right after the event. Through the UAV images, a high-resolution digital orthophoto map (DOM) and a digital surface model (DSM) have been obtained. The image has a ground resolution of 10–15 cm and covers an area of 21 km^2 (Fig. 3b). The image was compared with the pre-sliding Gaofen-2 image (recorded on April 8th, 2017, Fig. 3a) to carry out detailed geomorphic mapping and analyze the landslide geomorphological characteristics (see "Geomorphological characteristics and future hazard estimation" section). Due to the emergency condition, ground control points to improve the precision of DOM and DSM could not be set-up. However, by comparing the UAV data with the UAV-based LiDAR data provided by the Digital Green Land Ltd., a very good fit has been found. Unfortunately, the LiDAR data only cover a small part of the deposition area, thus they could be only used for data verification.

(2) Volume and depth calculation using pre- and post-sliding DEM

In order to infer the topographic changes and to estimate the landslide volume, the pre-sliding topographic map at 1:10,000

Table 1 Summary of the available data

Data	Resolution	Date	Data source
Before disaster			
Topographic map	1:10,000	2014	Sichuan Bureau of Surveying Mapping and Geoinformation
Geologic map	1:200,000	1975	Tang et al. (1991), and Li Yong (unpublished data)
Google Earth image		2003.08.18	Google Earth (Landsat-7)
Gaofen-2 image	0.8 m	2016.02.09	Chinese satellite Gaofen-2
Gaofen-2 image	0.8 m	2017.04.08	Chinese satellite Gaofen-2
InSAR		2015.06.20–2017.06.17 2016.04.28–2017.07.02	ALOS-2 SAR image provided by Prof. Liao Mingsheng from Wuhan University
During disaster			
Rainfall		2017.05.01–2017.06.23	Nearby rainfall station
Seismogram		2017.06.24	Maoxian seismic station
After disaster			
UAV image	0.15 m	2017.06.26	SKLGP
LiDAR	0.15 m	2017.06.25	Digital Green Land Ltd
GBSAR	Sub-millimeter	2017.06.29–2017.07.04	SKLGP

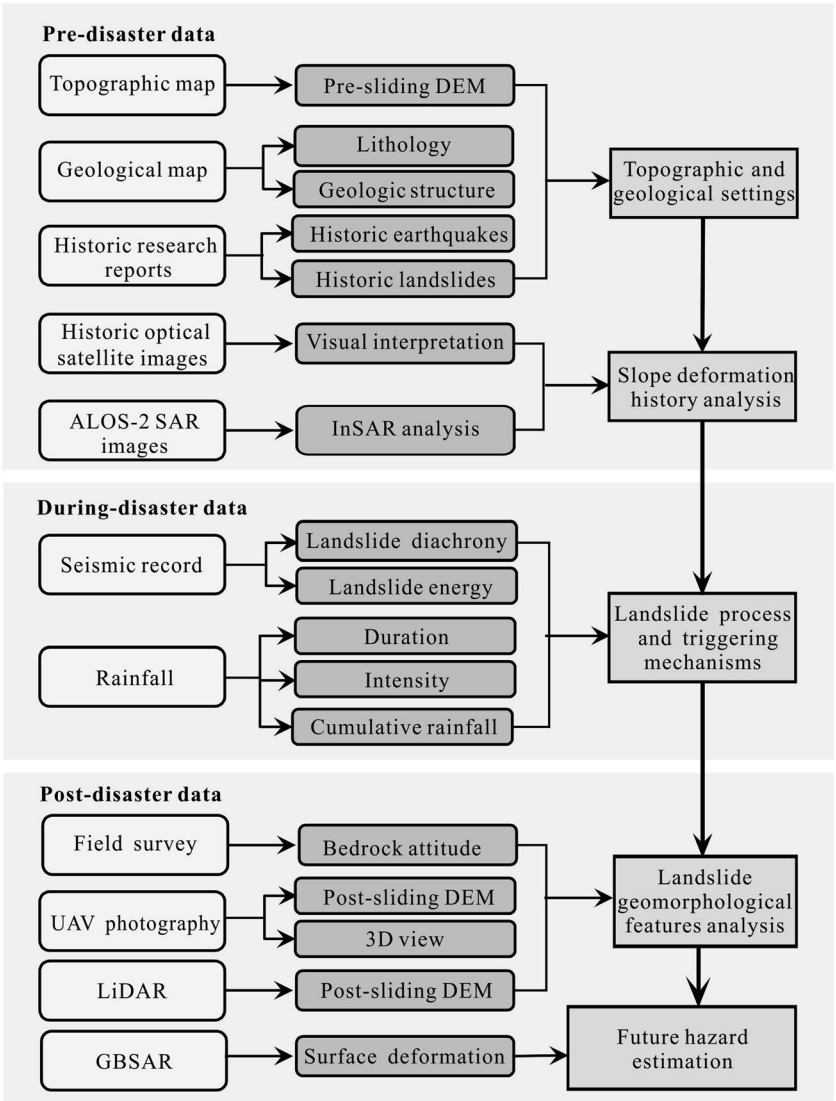

Fig. 2 Flowchart indicating the available data and the general methods

scale has been acquired. The map was prepared using stereo images of Cartosat-1 (2.5 m resolution) recorded in 2006 and of Pleiades (0.7 m) recorded in 2013. A pre-sliding DEM (about 1 m accuracy) has been generated using this topographic map. The pre-sliding DEM has then been compared with the post-sliding UAV DSM (10–15 cm resolution) to calculate the source mass volume and the deposition volume of the landslide using a cut-fill tool on the ArcGIS platform. Simple raster calculation, as the elevation difference between the pre-sliding and post-sliding DEMs, were used to estimate the depth of the landslide material ("Geomorphological characteristics and future hazard estimation" section).

(3) InSAR data interpretation

After the Xinmo landslide, several specialists have been working to detect any pre-failure deformations that could have been captured by InSAR data. For instance, Professor Zhenhong Li's team from Newcastle University, UK, collaborated closely with researchers from Chengdu University of Technology (in particular with the SKLGP), Tongji University, China Academy of Space Technology and Wuhan University (China) to utilize satellite radar technologies to identify the source area and boundaries of the landslide and, more importantly, to detect and monitor its pre-event movements COMET 2014 news 2017, UNISDR and China Daily), indicating the feasibility of landslide early warning systems. Multi-temporal images were collected to explore the deformation features of the source area before the landslide through the synthetic aperture radar interferometry (InSAR) time analysis technique, as shown in "Deformation history of the landslide" section.

(4) Spectral analysis of the landslide-generated seismogram

Recent studies have demonstrated that seismic monitoring is an effective technique to detect landslide events (e.g. Allstadt 2013; Chen et al. 2013). A seismogram of the Xinmo landslide was recorded at the Maoxian MXI broadband seismic station, about 43 km apart in SSE direction (azimuth 157.1°). The raw data provided by Prof. Xinghui Huang from China Earthquake Networks Center have been used to perform a spectral analysis,

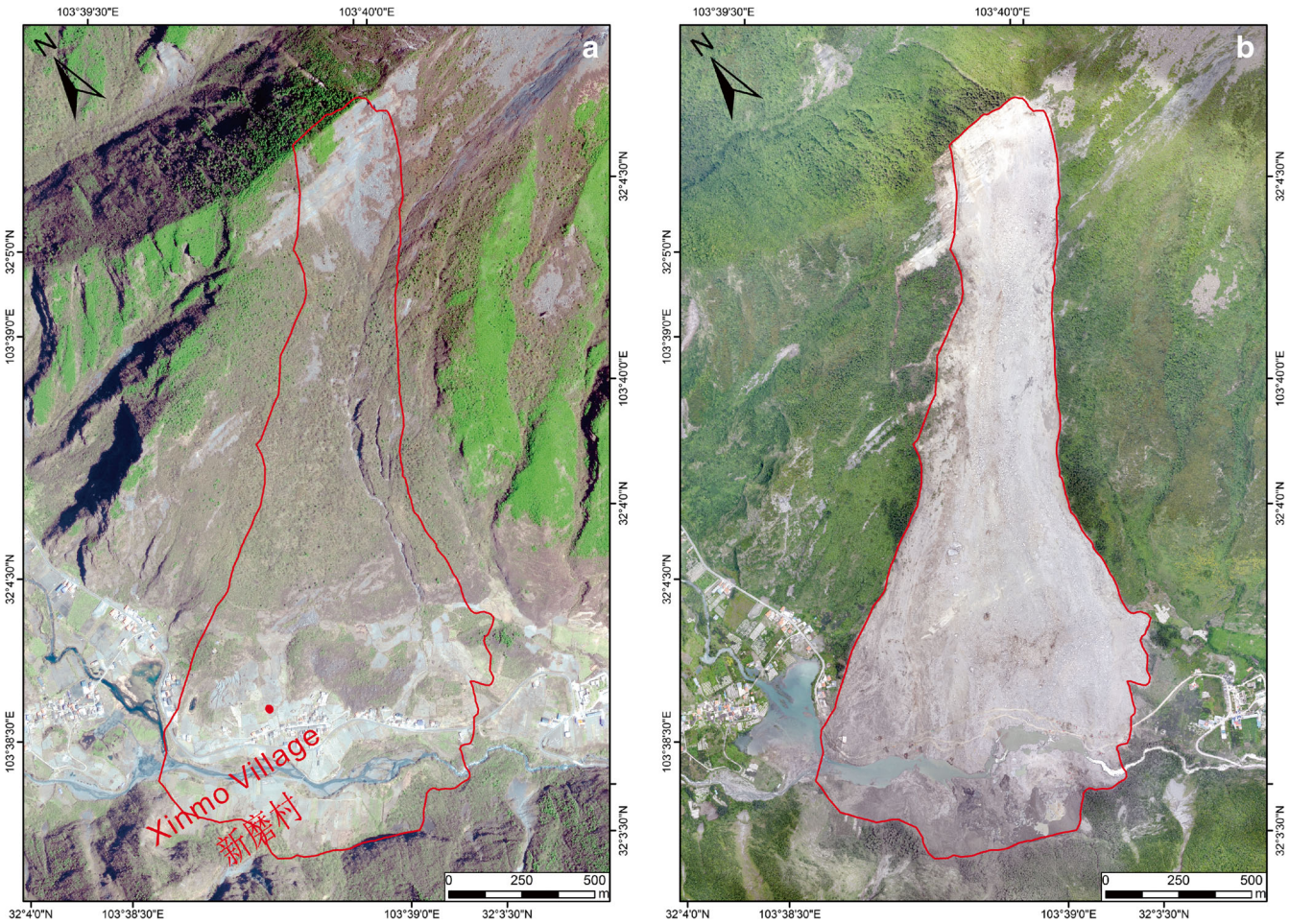

Fig. 3 Pre-sliding image from Chinese Gaofen-2 taken on April 8th, 2017 (**a**) and post-sliding image taken by UAV on June 26th, 2017 (**b**)

through which the initiation of the landslide, the travel time, the impact velocity and the displaced mass have been estimated ("Kinematics and failure mechanism analysis" section).

(5) Post-sliding deformation monitoring

As will be discussed in "Landslide-affected surrounding areas" and "Hazard assessment of the landslide-affected areas (IV-VI)" sections, the landslide event affected the stability of various rock and debris masses just beside the source area and the landslide channel boundaries. The use of a total station monitoring type is limited by the local topographic conditions. Thus, to monitor their possible deformation and to evaluate the residual hazard in the area, an IBIS-L ground-based synthetic aperture radar (GBSAR) was installed on June 29th, 2017.

Deformation history of the landslide

Due to the inaccessible position of the landslide source area, pre-failure deformation phenomena could not be observed, neither by locals nor by professionals through conventional survey methods. Remote sensing techniques are extremely useful in this case to identify the pre-failure deformation features. According to the Google Earth image (August 18th, 2003) in Fig. 4, an area of exposed bedrock, three macroscopic cracks along the sliding direction (CR1 to CR3) and two (CR4 and CR5) along the mountain ridge could be identified in the source area. The exposed bedrock is likely to be the scarp of the old landslide caused by the 1933 Diexi earthquake, as several other similar landslides have been proven to be induced by the same earthquake in the area, as shown by Fig. 1 (Wang et al. 2008; Ling 2015). The existing cracks suggest that the slope had been already gravitationally deformed and was prone to future failure long time ago. However, the Chinese Gaofen-2 satellite high-resolution image (April 8th, 2017) shows that the cracks did not further develop after 2003 (Fig. 5). This suggests that the 2008 Wenchuan earthquake did not enhance the slope deformation evidently. Figure 6 shows an image of the source area of the landslide after failure taken by the UAV. Comparing Figs. 5 and 6, it can be clearly seen that the western and eastern flanks of the source area were already bounded by CR1 and CR3 before failure. CR1 developed into the western steep scarp for a height of about 40 m.

The catastrophic Xinmo landslide attracted broad attention from research teams with InSAR expertise in China and abroad, who worked on the detection of possible slope deformations before the event and released very quick assessments; among them: Prof. Li Zhenhong's team from Newcastle University, UK

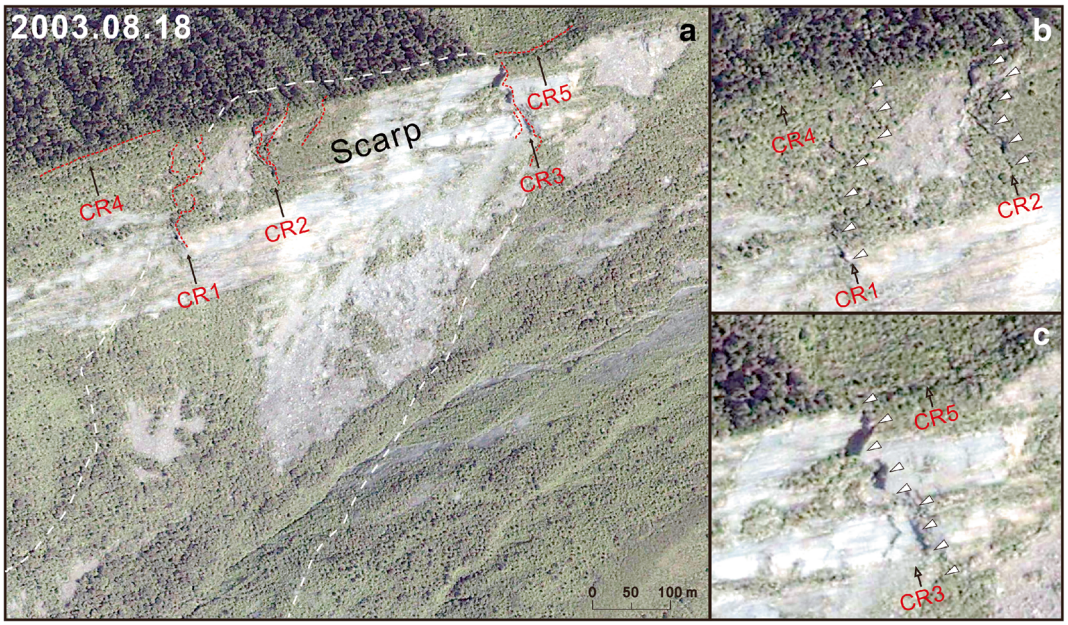

Fig. 4 The source area before the landslide event with the location of macroscopic cracks (Google Earth image, August 18th, 2003)

(COMET 2014 news 2017), the team of TRE ALTAMIRA Company, Italy (TRE ALTAMIRA, Precursor of Maoxian Landslide Measured from Space 2017), Prof. Lin Hui's team from Chinese University of Hong Kong (HK, China), Prof. Liao Mingsheng's team from Wuhan University (China), Prof. Zhang Qin's team from Chang'an University (China).

To detect the deformation history of the landslide with InSAR technology, we have processed the pre-event Sentinel-1 C-band data, as using its short wavelength is easy to detect the small deformation signal before the landsliding. Interferograms between images acquired on 08th April 2017 and 14th May 2017, 14th May 2017 and 19th June 2017 are shown in Fig. 7a, b, respectively. As can be seen from Fig. 7a, the source area indicated by the yellow arrow did not experience an evident displacement between 08th April 2017 and 14th May 2017. Compared with Fig. 7a, the source area showed in Fig. 7b underwent clear information during the period from 14th May 2017 and 19th June 2017 (5 days before the landslide). Accordingly, it can be inferred that significant deformation of the source area mainly occurred after the middle of May 2017. Similar results were obtained by other InSAR team [(COMET 2014 news, 2017, (TRE ALTAMIRA, Precursor of Maoxian Landslide Measured from Space n.d.)] using the Sentinel-1 data, showing that there is apparent deformation occurring before the landslide.

Geomorphological characteristics and future hazard estimation

According to the terrain and the geomorphological features, the Xinmo landslide site can be divided into three major zones: the source area (zone I), the track (transportation, zone II), the deposition area (zone III), see Fig. 8. In the track, a subdivision can be made between a central flow path and lateral abrasion areas. Adjacent to the landslide boundary, due to the dynamic action and to the unloading caused by the moving mass, fresh cracks formed and evident deformations occurred. More specifically, three landslide-affected areas with significant hazard have been identified, namely: a potentially unstable rock mass on the east of the source area (zone IV in Fig. 8), a potentially unstable rock mass on the west of the source area (zone V), and a displaced and deformed debris mass on the west side of the track (zone VI), just below the rock mass (V). In the following subsections, the landslide area and the landslide-affected areas are described in detail.

The major sliding zones (I–III)

Source area (I)

The source area is located at the very top of the slope, where the ridge reaches an elevation of 3431 m a.s.l, and it extends downslope to an elevation of about 3100 m. It covers less than 0.1 km^2, about 260 m along the slope direction and 370 m transversally. By comparing the pre- and post-sliding DEMs, the mobilized rock material was calculated to be in average 46 m thick, with a volume of 4.46 million m^3. Two sets of structural planes were crossing the rock mass: a sub-vertical set of discontinuities with attitude N 44 °E / SE ∠ 84° and an inclined set with attitude N 46° E / NW ∠ 47°. The mass slid along a bedding plane (attitude N 80° W / SW ∠ 47°), leaving the bedrock exposed, with sub-vertical discontinuities marking the lateral boundaries (Fig. 9).

As described earlier, the area experienced several strong earthquakes in the past hundred years. This likely contributed to the formation of a large quantity of cracks and fractures within the rock mass, which are evident on the surface (Figs. 4 and 5). Furthermore, from the high-resolution post-event UAV image and photo (Figs 6 and 9a), it is also possible to identify signs of weathering in the top part of the exposed sliding surface and cavities in the lower part, suggesting carbonate dissolution and significant rainwater infiltration and groundwater mobility. The images also show several cracks on the mountain ridge, which

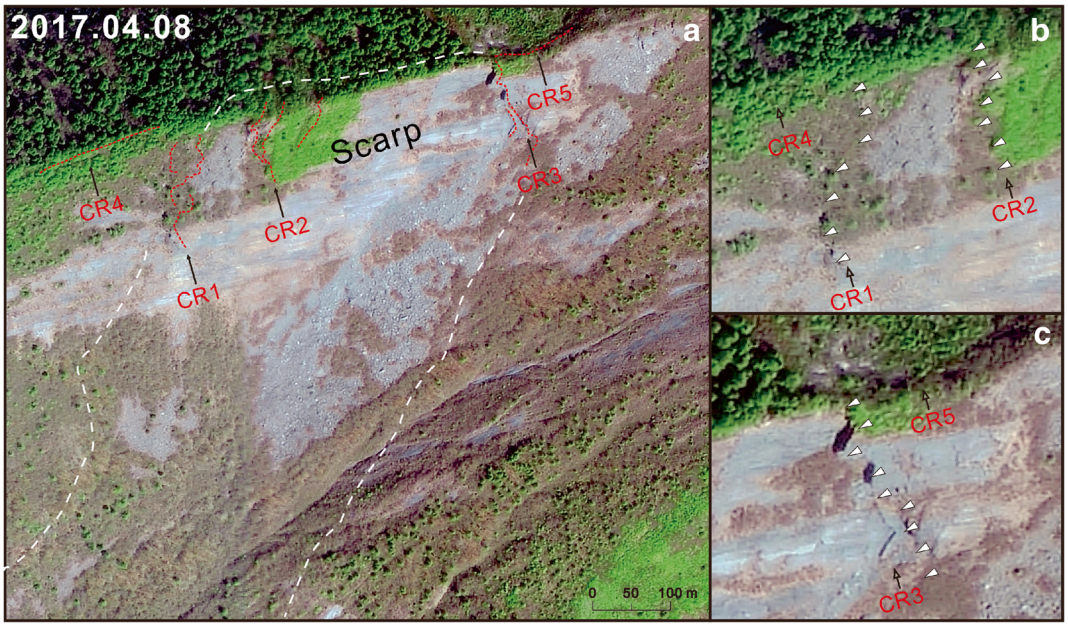

Fig. 5 The source area before the landslide event with the location of macroscopic cracks (Chinese Gaofen-2 satellite image, April 8th, 2017)

were already interconnected to some extent before the landslide. The presence of these cracks is a predisposing factor to failure in case of heavy rain infiltration, as they can be filled with water and generate hydrostatic pressures which would pull the blocks apart and facilitate their collapse.

Landslide track or transportation area (II)

The landslide track spans from an elevation of about 3100 m a.s.l. to an elevation of 2650 m. The rock mass slid along the track with very high kinetic energy and mobilized the pre-existing loose deposits by scraping, entraining and pushing them downwards. The abrasion exerted by the sliding material formed a U-shaped channel, about 410 m wide, 30 m deep and 700 m long. The total volume of the mobilized loose material is estimated to be 4.3 million m^3.

Within the track, two sub-areas can be identified: a central flow path (II-1) and two lateral abrasion areas (II-2), see Figs. 8b and 10. The pre-existing loose material was entrained by the rock mass and pushed downwards with it. At a later stage, some additional material (0.7 million m^3), resulting from local collapses in the

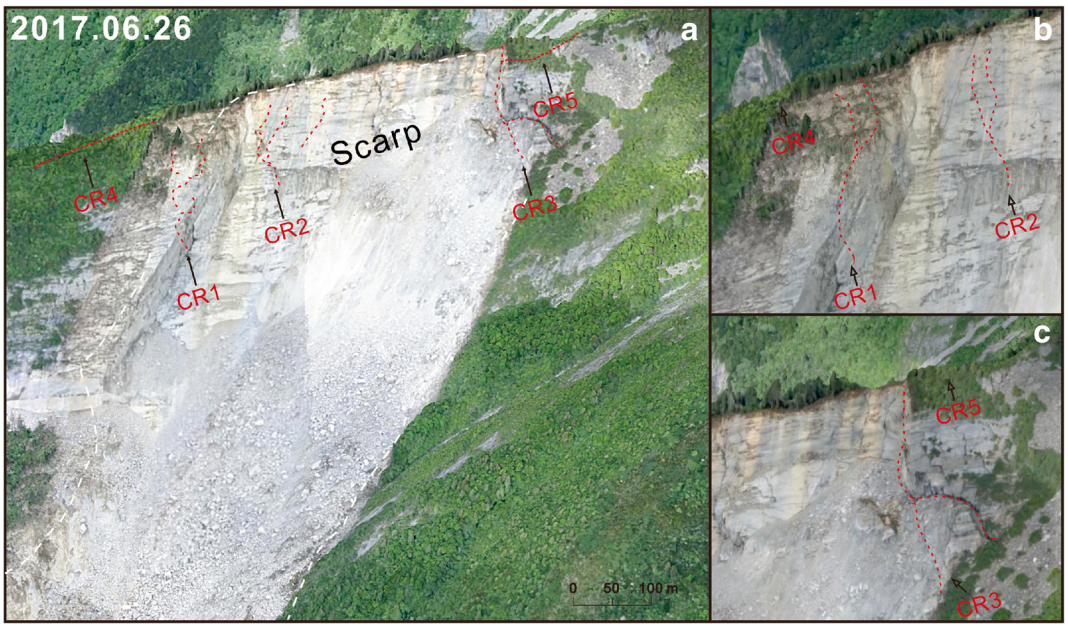

Fig. 6 Three-dimensional reconstruction of the source area after the landslide event (UAV image recorded on June 26th, 2017)

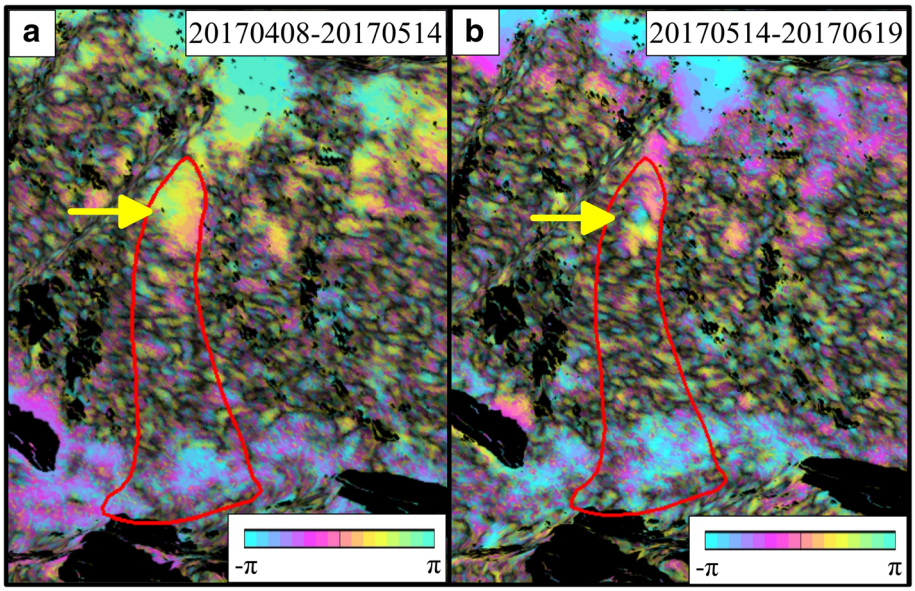

Fig. 7 Differential interferograms of the landslide with Sentinel-1 data

source area, travelled along the newly-formed channel and deposited in its lowermost part.

It is worth noting, in Fig. 10, that the deposits in the main flow path are not symmetrical: the west side has a lower height than the east side. This can be due to the pre-existing terrain topography, which deviated the sliding movement eastwards. The lateral abrasion areas (II-2 in Fig. 8b, located on both flanks of the U-shaped channel, are defined as the areas which only suffered the scraping action of the moving mass, but were not covered by secondary deposition due to their higher slope angle.

Deposition area (III)

Before the landslide event, the area now occupied by the new landslide deposits was actually already partly covered by the deposition fan of a landslide induced by the 1933 Diexi earthquake (Figs. 1 and 8). During the recent event, the mass travelled along the track acquiring huge momentum and was thus able to displace the pre-existing deposit. A large area of exposed bedrock, once covered by the old deposition fan, is actually clearly visible (Figs. 8 and 10). Meanwhile, additional debris from the two sides of the channel was mobilized and it accumulated on top of the previous deposits. The new landslide deposition area is shown in Figs. 8 and 10. The deposits blocked the Songping gully and formed a dammed lake.

After the event, the summit of the deposition area reaches about 2800 m a.s.l., while the toe lies at an elevation of 2290 m a.s.l. The deposit is generally more than 10 m thick, it covers an area of about 1.19 km^2 and its volume is estimated to be about 12 million m^3. Thus, the total volume mobilized in the Xinmo event, including the deposits in the track, has been quantified in about 13 ± 1 million m^3.

The field investigation and the UAV image show that the rock mass originating from the source area crushed and broke down in the avalanching process and finally accumulated in the fluvial valley in the form of a highly fragmented debris, although some very large blocks reached the deposition area intact. The field investigation, in fact, revealed the presence of some very large blocks, the largest of which is some 40 m wide and has an estimated volume of 50 thousand m^3 (Fig. 12a, e). Most of the large blocks were deposited in the area between the lowest part of the track and the Xinmo Village, while the relatively small-sized boulders and the debris continued moving until the farthest bank of the Songping gully. These deposits exhibit the typical inverse sorting of other flow-like landslides with high-velocity and long runout (Hungr et al. 2014). On the basis of the field investigation, aerial images interpretation and geological analysis, the geological longitudinal profile of the Xinmo landslide could be drawn (Fig. 11).

Landslide-affected surrounding areas

The dynamic action and the unloading caused by the landslide led to the formation of fresh cracks and to mass deformations. Three potentially unstable areas have been identified through the high-resolution UAV image and the in situ investigation. Two rock masses with new cracks have been found on the west flank (IV) and on the east flank (V) of the source area. Another potentially unstable mass, mainly composed of debris, was detected just downslope of the west side rock mass (VI). Their positions are shown in (Figs. 8b and 12).

Rock mass in the east flank (IV)

This rock mass is located on the east-upper part of source area. It lies at an elevation between 3465 m (upper edge) and 3371–3403 m a.s.l. (front edge). It is 106 m long, 90 m wide and about 20 m thick, with an estimated volume of 0.2 million m^3 (Fig. 12a, c). Through the high-resolution remote-sensing images, it was identified as a thick rock plate, with several crack distributed on the surface. Its degree of weathering is higher than that of the rock mass (V) on the opposite flank. The front and west sides of the rock mass (IV) are exposed, while the east side seems well bonded

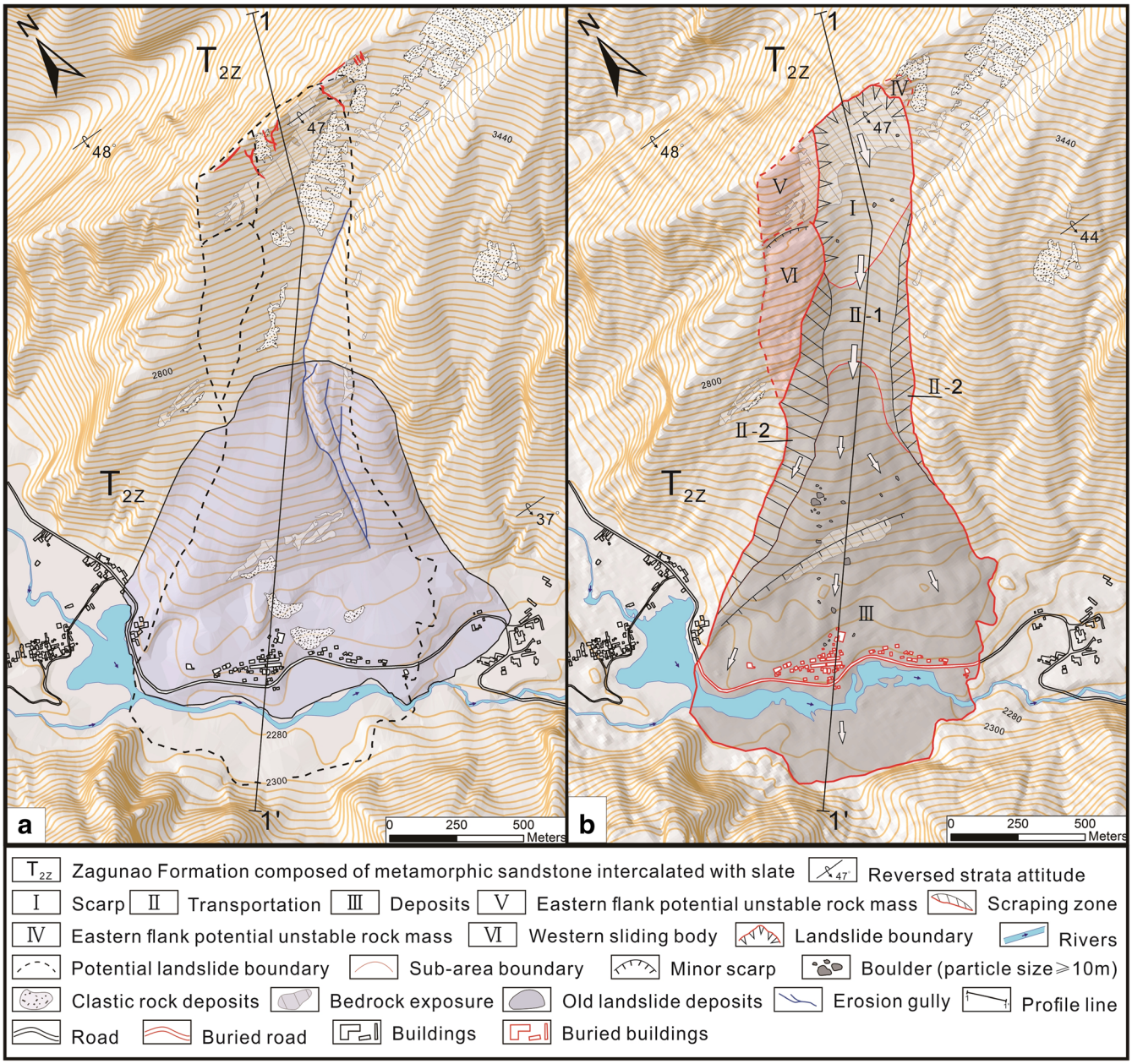

Fig. 8 Pre-sliding (**a**) and post-sliding (**b**) geomorphic maps of the Xinmo landslide, indicating the different zones of the landslide

to the bedrock. The overall failure of the rock mass seems not likely in short time, while small-scale rock falls, due to the existing crack patterns, might occur.

Rock mass in the west flank (V)

This rock mass is exposed on three sides and its stability fully relies on the connection with the bedrock (Fig. 12a, b). It is a large block with seemingly intact structure. Its upper edge reaches an elevation ranging from 3266 to 3351 m a.s.l., while the front edge lies at about 3073 m. Its height, width and thickness are about 230, 220, and 35 m, respectively, with an estimated volume of 1.8 million m^3. As presented in Figs. 5 and 6, CR4 exists in this zone both before and after the landslide event. Nonetheless, strong bonds between the potential sliding plane of the rock mass and the bedrock were found during the investigation. Hence, this rock mass is supposed to be relatively stable and perhaps would not fail in short time.

Debris mass in the west flank (VI)

A large-scale deformation just below the rock mass (V) on the west flank was detected through the interpretation of 3D UAV image (Fig. 12a). The mass has a trapezoidal shape, with an upper width of 250 m, a lower width of 100 m, and a length of 450 m. The average thickness is evaluated in 58 m, with a volume of 4.55 million m^3 (Fig. 12d). Behind the upper edge of the mass, a tension trough, 43 m wide and 20 m deep, was formed along the strike

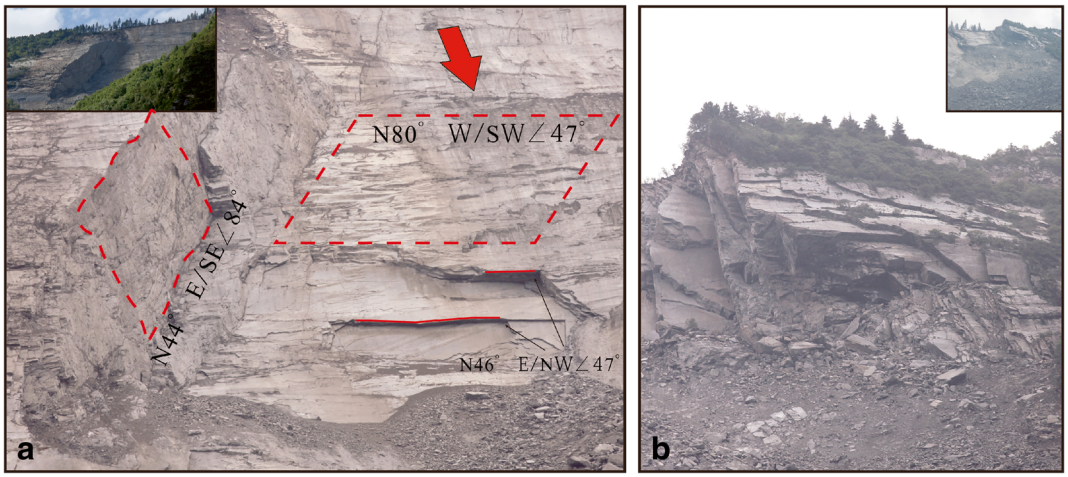

Fig. 9 Photos showing the source area of the Xinmo landslide. Scarp and west boundary (**a**). East boundary (**b**)

direction of the strata. A second trough is found in the front of the mass, 54 m long and 10 m wide. The mass is mainly composed of debris material.

Frequent small slides on the exposed front and east sides occurred after the landslide event. During the emergency rescue operations, the mass was believed to be in incipient failure state and had received considerable attention from both the specialists and the government. Based on the available information, the debris mass seems to have been displaced by the shearing and dragging action of the landslide rock mass, which had already achieved a considerable kinetic energy. However, the mass stabilized after a movement of about 40 m as it encountered a natural obstacle. Figure 12a shows indeed a large exposed plane with strata attitude of N 46° E / NW ∠ 47°. This anti-inclined plane extends from the East-upper part of the slope, crossing the front part of the landslide source area, to the front edge of the displaced mass. The plane generated a topographic depression in the front of the landslide source area (Fig. 12a).

Hazard assessment of the landslide-affected areas (IV–VI)

In order to provide a reliable evaluation of the stability condition and of the residual hazard in the landslide area and its surrounding, with the aim of ensuring the safety of people near the landslide deposition area and preventing secondary disasters, a quick installation of efficient emergency monitoring stations has been necessary. The use of a total station monitoring type is limited by the local topographic conditions, thus an IBIS-L ground-based synthetic aperture radar (GBSAR) was installed on June 29th, 2017 with the main scope of monitoring the rock mass (V) and the debris mass (VI) on the west flank of the landslide.

In order to carry out a simplified but efficient analysis, 16 monitoring points have been selected as representative of the

Fig. 10 An overview photo of the Xinmo landslide showing the source, transportation and deposition areas

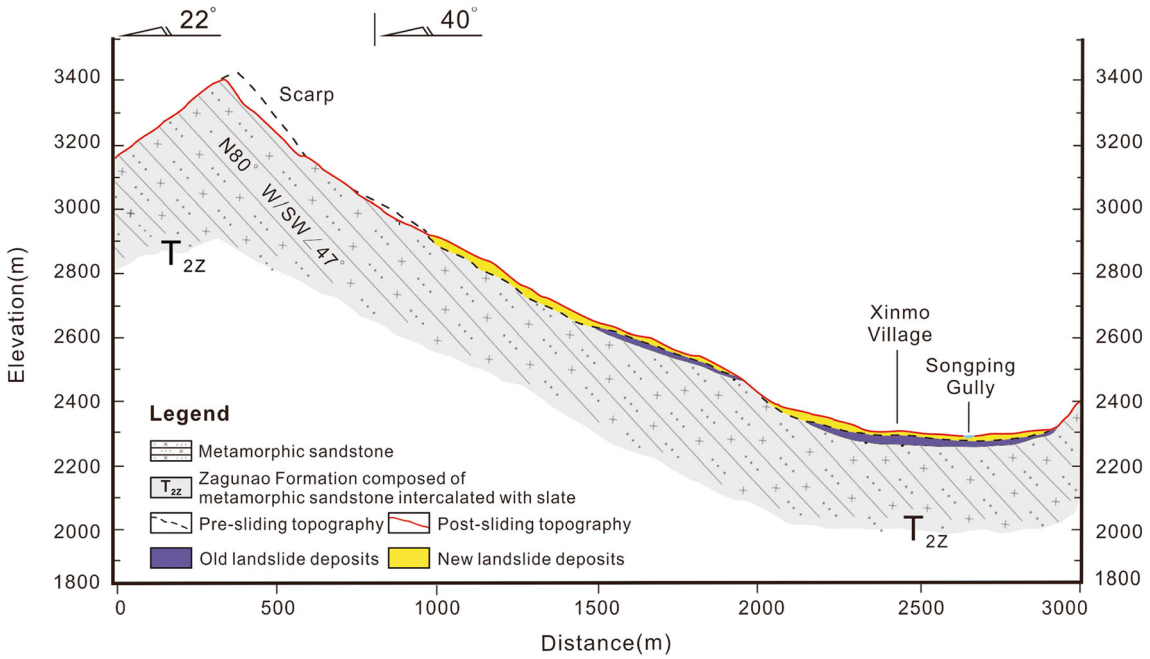

Fig. 11 The geological longitudinal profile of the Xinmo landslide

deformation patterns of different regions. Their positions are shown in Fig. 13. The displacement data of these representative points collected in the first days of monitoring are shown in Fig. 14. On the basis of these data, the following preliminary observations can be made:

(1) *Bedrock.* Points P27 and P28, located on the exposed bedrock on the scarp were used for the baseline correction and error analysis. The monitoring data did not show significant displacements, as the values fluctuated near the zero line within the error range of the acquisition system. A periodic fluctuation in the order of 10–20 mm was anyway observed between 8:00 a.m. and 15:00 in the first three monitoring days (sunny days), while it was not significant in the following 2 days (rainy days). This suggests that the monitoring system is influenced by the environmental conditions (temperature, humidity, atmospheric pressure). However, as the same fluctuations are observed in all points, including the stable ones, the displacements can be promptly corrected to account for these fluctuations.

(2) *Rock mass (V).* The monitoring points P11 and P12 are both located in the front part of the mass. They show cumulative displacements of opposite sign: −83 mm in P11, i.e. towards the bedrock, and +18 mm in P12, i.e. departing from the bedrock. This might indicate that the rock mass is still in a phase of deformation adjustment and is relatively stable.

(3) *Debris mass (VI).* Within the first five monitoring days, the averaged cumulative displacement of six monitoring points (P2, P6, P7, P8, P9, P10) located in the Eastern and rear part of the mass reaches +93 mm. Among these points, P8 shows the maximum value (+145 mm), corresponding to an average deformation rate of about 30 mm/day. In the front part of the mass, the average cumulative displacement of six monitoring points (P1, P2, P4, P5, P13, P14) reaches +36 mm. Among these points, P5 shows the maximum value (+119 mm), corresponding to an average deformation rate of about of about 25 mm/day. The fact that the rate is higher in the front part than in the rear part suggests that the debris mass is still compressing against the structural obstacle which constrains its movement. On July 4th, a long-duration rainfall event occurred. Nonetheless, the monitoring data did not show significant trend changes, which might suggest that the internal strains are still the dominant deformation mechanism. However, as the absolute deformation rate is still significant in the front part of the mass, it cannot be excluded that further events or the progressive failure of the constraint might trigger dramatic displacements of the whole mass, thus a continuous monitoring remains essential to detect early signs of incipient failure.

Kinematics and failure mechanism analysis

Kinematic analysis from a broadband seismic network

The Xinmo landslide event generated a seismic shaking detected by several seismic stations, the closest one being the Maoxian MXI station, about 43 km apart from the landslide site (Xu et al. 2017). The event had an estimated Richter magnitude M_L = 2.3 and a landslide seismic magnitude Lm = 3.6 (after Lin et al. 2015). The seismogram recorded at the MXI station exhibits similar features along the three directions, thus the detailed analysis of just a single component is reported in this work (Fig. 15a). The recording begins at 05:38:35 local time of June 24th, 2017. Due to the close distance and the magnitude of the event, the whole signal clearly emerges from the background, about 26 s from the beginning of the recording (05:39:01 local time, line I in Fig. 15) and lasts for about 121 s (line IV).

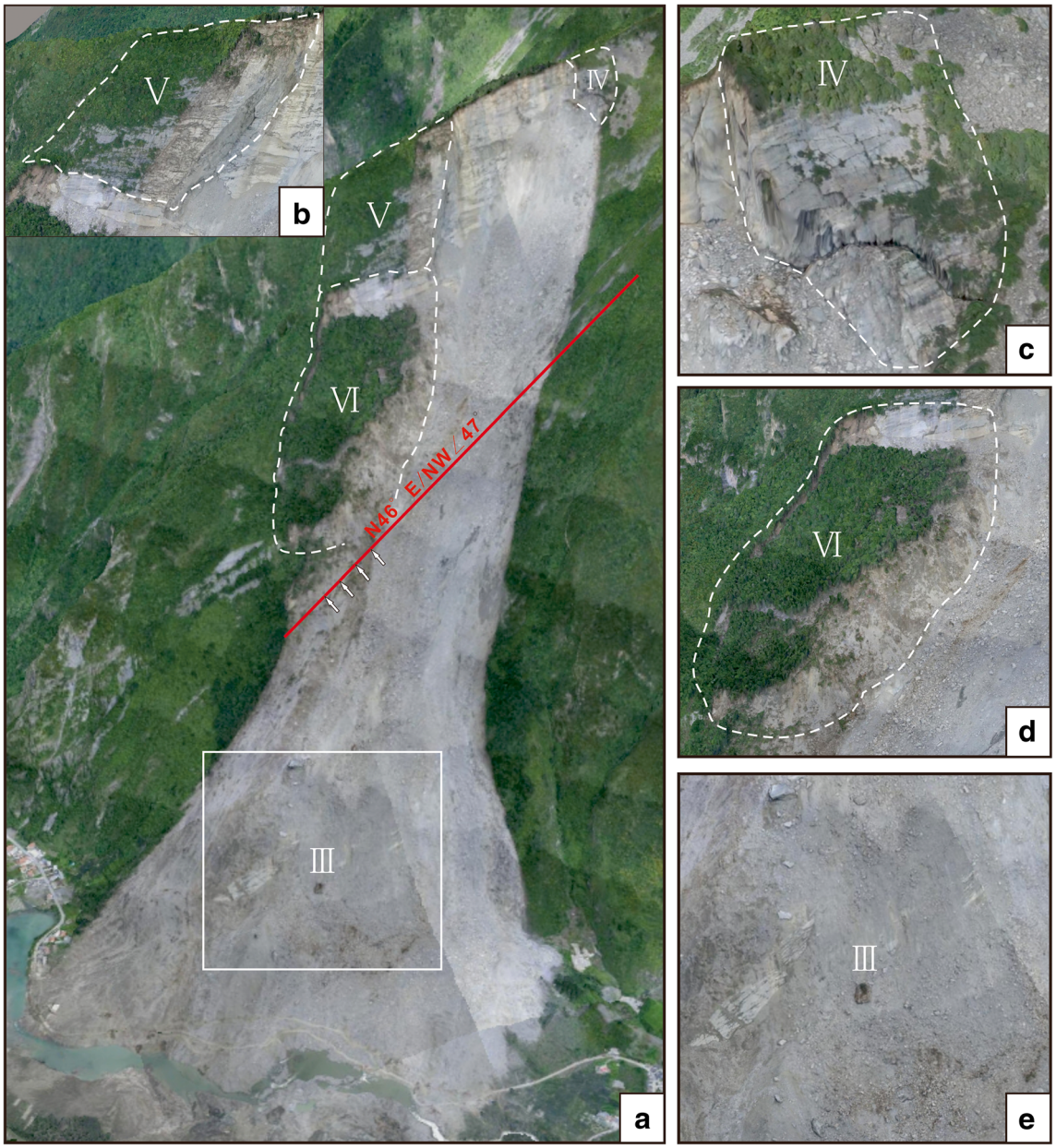

Fig. 12 The 3D view of the Xinmo landslide and the affected surrounding areas

Landslide-generated waves contain specific features, namely a low-frequency component produced by the broad cycle of unloading and reloading of the solid Earth induced by the bulk acceleration and deceleration of the landslide mass (Ekström and Stark 2013), and a high-frequency component, distributed in time, which results from the complex momentum exchanges between landslide debris clasts and the bed as it is sliding and impacting in the deposition area (Yamada et al. 2012; Lin 2015). The release of low frequency waves has been related to the initiation of rock avalanches (e.g., Lin et al. 2010; 2015; Yamada et al. 2012; Lin 2015; Coe et al. 2016).

In order to identify the frequency content of the waveform, the 2D time-frequency distribution spectrum has been obtained through the Hilbert transform (Fig. 15b). A time integration over the whole duration has been also performed to obtain a frequency-magnitude spectrum (Fig. 15c), from which the presence of distinct low-frequency and high-frequency components is apparent. The values $f = 2.73$ Hz and $f = 0.40$ Hz have been taken as representative of the characteristics of the signal in the high-frequency and in the low-frequency ranges, respectively. The magnitude of the signals at these two frequencies is plotted in Fig. 15d, e. The arrival of the low frequency component precedes the high frequency waves of several seconds. The former has a first important peak after about 15 s, probably when the rock mass full mobilization is achieved. The high-frequency component is negligible for about 10 s after the initiation, then maintains relatively low values for about 30 s before increasing first gradually and then more evidently (line II in the figure); it peaks at $t = 91.51$ s (line III) before decreasing quite sharply.

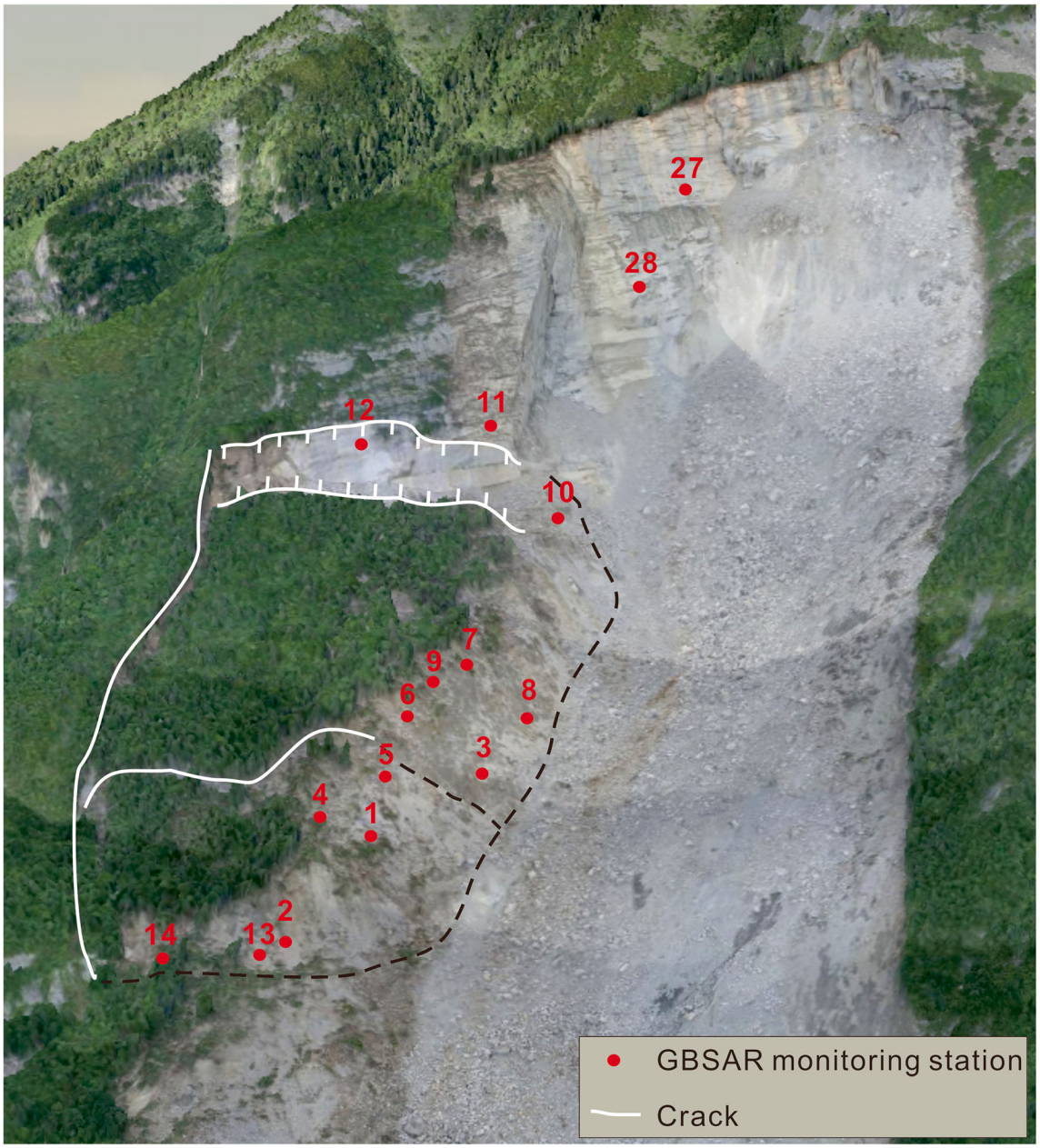

Fig. 13 Setting up of GBSAR monitoring points

It is possible that during the first few seconds after the full mobilization, the rock mass travelled as a whole, without significant crushing and entraining. When it reached the lower part of the track, having gained important momentum, it probably crushed intensely, and mobilized and entrained the loose material of the old landslide deposit. Most of this process, with large energy dissipation, roughly occurred in just about 15 s (between line II and line III), about 50 to 65 s after the landslide initiation. A significant low-frequency peak can be also noticed around $t = 70$ s (Fig. 15e, before line II) after the landslide mass probably slid over an area of exposed bedrock, generating an elastic rebound. This seems actually reasonable on the basis of the remote sensing images obtained before the landslide event (Figs. 8 and 12) which show indeed the presence of exposed bedrock in the lower part of the track. After the peak (line III, Fig. 15d), a quite sharp decrease of the high-frequency content can be seen. This reasonably corresponds to the impact of the material with the village and the river valley, while the subsequent waves (from line III to line IV) correspond to the deposition and the gradual stopping of the mass. The signal vanishes in the background noise (line IV) after about 121 s from the arrival of the first wave.

The source mass detached from the slope, accelerated and hit the Xinmo village in just about 60 s, after travelling for more than 2.5 km. An impact velocity in the order of 250 km/h can thus be estimated. Using the landslide seismic magnitude Lm, it is also possible to roughly estimate the sliding volume. In fact, an energy

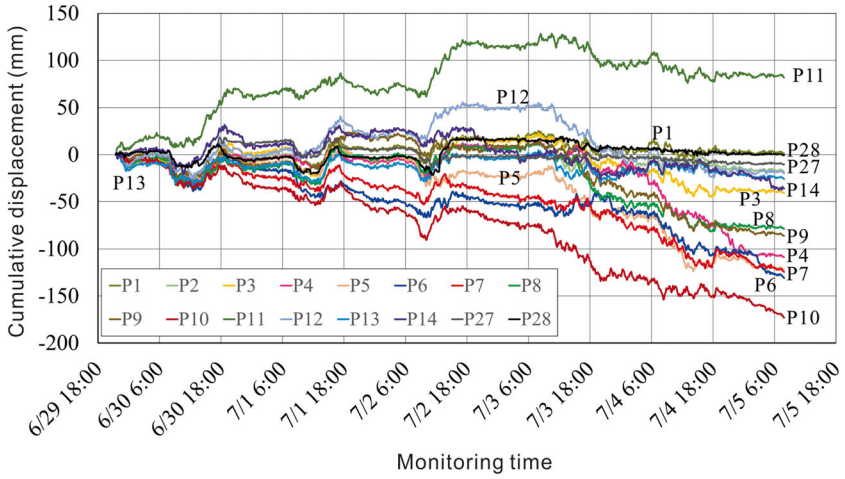

Fig. 14 Cumulative displacement curves of monitoring points in the west potentially unstable rock mass (VI) measured by GBSAR

release of 290 TJ can be evaluated (Lin et al. 2015), which can be related to the loss of gravitational potential energy of the mass travelling downslope. On this basis, with a reasonable assumption for the unit weight (20–23 kN/m^3), a mobilized volume in the order of 12–13 million m^3 can be estimated, which is very close to the evaluation based on remote sensing and in-situ investigation.

The accuracy of this simple calculation pushes in favor of the implementation of algorithms for real-time detection of landslide

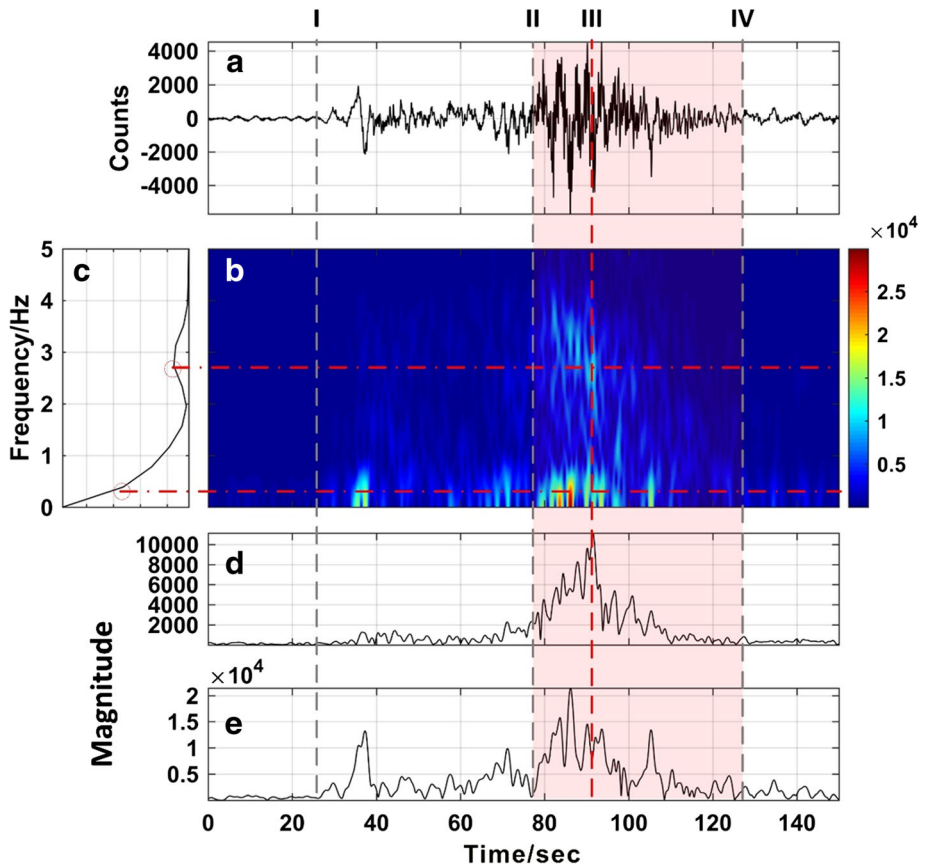

Fig. 15 Seismic signal of the Xinmo landslide event recorded by the Maoxian MXI station, vertical component (**a**); 2D time-frequency distribution spectrum (**b**); frequency-magnitude spectrum (**c**); time-magnitude spectrum at $f = 2.73$ Hz, representative of the high-frequency characteristics of the signal in the time domain (**d**); time-magnitude spectrum at $f = 0.4$ Hz, representative of the low-frequency characteristics of the signal in the time domain (**e**). The signal recording begins at (UTC) 2017-06-23 21:38:35 (i.e., 2017-06-24 05:38:35 local time) and the sampling interval is 0.01 s ($F_s = 100$ Hz). The lines I, II, III, and IV mark the progressive times $t = 26.41$ s, $t = 77.10$ s, $t = 91.51$ s, and $t = 127.30$ s, respectively

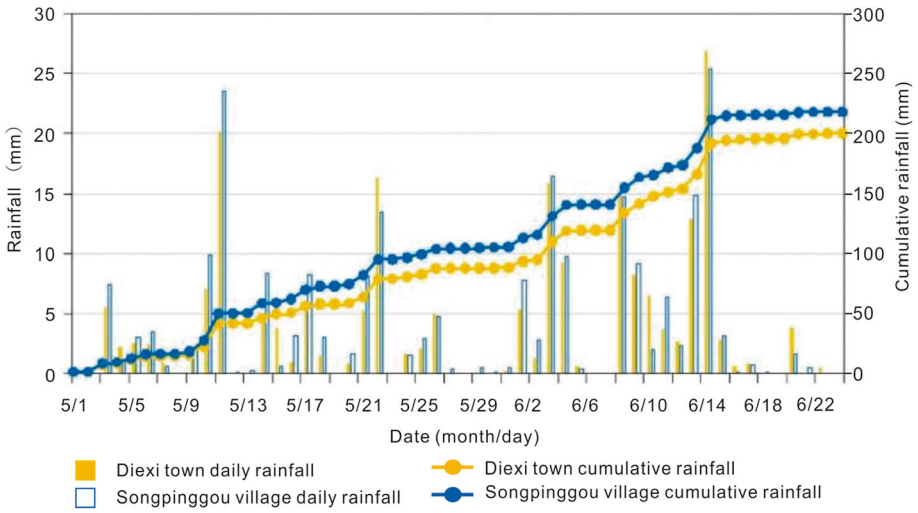

Fig. 16 Cumulative rainfall prior to the landslide occurrence in the Diexi town and Songpinggou village (provided by Prof. Yueping Yin)

events using the existing seismic network (e.g. Manconi et al. 2016; Chao et al. 2017) which could prove very helpful for the authorities to obtain, within minutes, quantitative information about the event magnitude, volume, mechanism and destructive power for rapid hazard assessment and emergency response.

Failure mechanism analysis

The occurrence of the Xinmo landslide is the result of a combination of predisposing and triggering factors. On the one hand, the interplay between geological, tectonic, seismic, physical and hydro-chemical processes produced a slide-prone condition. On the other hand, the hydrological condition triggered the dramatic failure.

Predisposing factors

The landslide occurred within the Zagunao Formation (T_2z), which is mainly composed of metamorphic sandstone and slate. It is characterized by a relatively low mechanical strength and well developed weak structural planes. The orientation and dip angle of the bedding planes is practically coincident to that of the hillslope, a condition which facilitates base sliding greatly. The landslide area falls at the intersection of two active faults—the Minjiang and the Songping faults (see Fig. 1), it has experienced extremely active tectonic movement and suffers high seismic activity, with the 1933 Diexi earthquake being the most destructive in the area. The frequent earthquakes contributed to the formation of new cracks and fractures in the rock mass and to the propagation and opening of pre-existing discontinuities. Tensile sub-vertical cracks particularly developed at the west and east boundaries of the source rock mass, providing a structural condition for the landslide initiation. Open cracks constituted a preferential flow path for the infiltration of rain water and accelerated the processes of physico-chemical weathering of the rock (Fig. 6), leading to a progressive reduction of its mechanical characteristics. In combination with this, the long-term gravity effect induced further crack propagation, eventually causing the source rock material to enter a state of incipient instability.

Hydrological trigger

The recordings of two nearby monitoring stations (see Fig. 16) showed that, between May 1st, 2017 and the time of the landslide event, the cumulative rainfall exceeded 200 mm. This value is significantly greater than the average rainfall in the same period in the area (information from Sichuan Meteorological Service, http://www.scqx.gov.cn/). Although the amount of rainfall during the days preceding the event was relatively small, a long-duration rainfall event occurred between June 8th and June 15th, with a cumulative rainfall of 80 mm and a daily maximum of 25 mm. Evidently, the Xinmo landslide was not triggered by a single, intense rainfall event, but rather by the consequence of long-duration, although less intense rainfall. Prolonged rainfall might have caused a slow but progressive build-up of hydrostatic pressures in the fractures and/or a persisting condition of significant hydrostatic pressures. This might have caused slow creep deformations at the boundaries and within the source mass. This led to crack propagation, which finally accelerated towards a dramatic failure. Indeed, the hypothesized mechanism would require a prolonged period of acting stress, which is compatible with long-duration rainfall events rather than with short episodes. However, even these latter (and even of low intensity) could be sufficient to trigger failure through a hydrostatic pressure build-up, if the effect of antecedent long-duration events had already caused the mass to be on the edge of failure. It is worth noting that the hydro-mechanical-temporal interplay suggests that the identification of rainfall thresholds for this mechanism is not straightforward.

Discussion

In recent years, several catastrophic landslides occurred in China (Huang 2009; Xu et al. 2009, 2010; Zhang and Yin 2013; Yin et al. 2016). Among them, the Wulipo landslide (Yin et al. 2016), which affected the village of Sanxi (Zhongxing Town, Dujiangyan City) on July 10th, 2013, leaving 44 dead and 117 missing, had similar characteristics to those of the Xinmo landslide discussed in this paper. In both events, the source mass originated on a mountain slope at high elevation, in an area covered by dense vegetation. Remote sensing and aerial images showed clear signs of fractures

and weakening in both areas, related to the action of strong earthquakes. Both in 1933 in Xinmo and in 2008 in Wulipo, the seismic intensity reached Level X during the Diexi and the Wenchuan earthquakes respectively. Furthermore, both landslides occurred rather suddenly, without macroscopically noticeable precursory signs.

Conventional geological hazard assessment based on in situ investigation is made difficult by the arduous topography in mountainous areas, thus the early detection and the implementation of precautional interventions are hardly feasible. This is a widespread issue in the field of hazard prevention and mitigation. We should treasure the tough lesson of these catastrophic events and pay extreme attention to preventing and mitigating hazards. Back to the key issue proposed in the Introduction section: "Is it possible to perform early recognition and warning of such kind of landslides, if so, how?", we encourage the research community and the professional departments to focus the efforts into the following directions and practical actions:

(1) To strengthen the research on the methods of early detection of hazards in high elevation source areas with the aid of all the available new technologies. Current research does show that the use of InSAR can be successful in detecting a wide range of deformation areas, while the use of LIDAR and UAV is well convenient in identifying fractures and sliding deformations. Large-scale implementation, as soon as possible, of these techniques for the early detection of hazards in mountainous areas is strongly recommended.

(2) To further develop the research on long-term effects of geological hazards in highly seismic areas, with the aim of assessing and mitigating the risk. Various case studies of strong earthquakes worldwide indicate that the impact of strong earthquakes in mountainous areas might last for hundreds of years (e.g. Korup 2005; Koi et al. 2008; Wei et al. 2014). In China, for instance, many large-scale geological hazard events occurred in the 2008 Wenchuan earthquake area and many are still likely to occur (Tang et al. 2009; Fan and Huang 2013; Yu et al. 2014). The Xinmo Village landslide of June 24th 2017 is directly related to the Diexi earthquake which occurred more than 80 years ago! Hence, we should strengthen the research on geological hazards and work intensely on the development of preventive countermeasures and warning systems, especially in areas with intense seismic activity.

(3) To carry out comprehensive investigations of geological hazards in landslide-prone exposed areas with the use of all possible means. This includes the cooperation among expertise related to land surveying and mapping, meteorology, seismology, and so on. Data sharing among scientific and professional departments is warmly encouraged in order to achieve reliable early identification, monitoring, warning, alarming, emergency intervention and treatment, and assessment and mitigation of secondary hazards. The various expertise must work collaboratively, share data and exchange information. We argue that a dedicated hazard prevention and mitigation department should be established at the earliest convenience, the mission of which would be to coordinate and integrate resources such as information, equipment and manpower, to set up big data centers and platforms, to carry out comprehensive research on geological hazard prevention, to promote the industrialization and practical application of innovative technologies and achievements, and finally to comprehensively enhance our capacity of preventing and mitigating geological hazards.

Conclusions

This paper presents a preliminary investigation on the recent catastrophic Xinmo landslide. Visual interpretation of multitemporal remote sensing images (including the UAV image) were used to analyze the deformation history of the landslide. The images revealed several cracks on the mountain ridge, which were interconnected to some extent already before the event. This has been recognized as a predisposing factor to failure, as they constitute a preferential flow path for the infiltration of rain water and can accelerate the processes of physico-chemical weathering of the rock. The cracks are thought to have been formed during the 1933 Diexi earthquake. In this area, this earthquake reached an intensity of Level X and triggered a large number of landslides.

Synthetic aperture radar interferometry (InSAR) provides an effective way to help identify potential landslides. It can give information on the extent and on surface displacements of landslide-prone source areas, considered precursors of sliding. The differential interferograms of ALOS-2 SAR data from periods 2015.06.20–2017.06.17 and 2016.04.02–2017.03.02 showed deformation of the landslide source area taking place after March 2017.

The very high-resolution UAV image (0.15 m resolution) and field investigation were employed to analyze the geomorphological characteristics of the Xinmo landslide. The landslide could be divided into three major areas (source, transportation and deposition) and three surrounding affected areas (potential unstable blocks). The volume of the source material and the deposition mass were calculated to be 4.3 million and 13.0 million m^3 respectively by comparing pre- and post-sliding DEMs. The first monitoring data based on GBSAR measurements were interpreted to assess the potential residual hazard in the landslide area. Landslide-generated seismogram traces at the nearby Maoxian broadband seismic station have been used to identify the initiation and travelling times of the landslide and to obtain a quick estimation of the displaced mass.

The occurrence of the Xinmo landslide has been shown to be the result of a combination of predisposing and triggering factors. On the one hand, the interplay between geological, tectonic, seismic, physical and hydro-chemical processes produced a sliding-prone condition. On the other hand, the hydrological condition triggered the dramatic failure. Prolonged rainfall might have caused a progressive and persisting build-up of hydrostatic pressures within the existing cracks, possibly causing slow creep deformations leading to crack opening and propagation, which finally produced the mass collapse.

Early recognition of potential instabilities in mountainous areas is hardly feasible through conventional geological hazard assessment based on in situ investigation. Nevertheless, this case study showed that the use of modern technologies and the collaborative work of experts and professionals can prove successful in identifying potential hazards and performing quick assessments. The establishment of a dedicated hazard prevention and mitigation department to coordinate and integrate resources and comprehensively enhance our capacity of preventing and mitigating geological hazards is warmly welcomed.

Acknowledgements

After the occurrence of the June 24th Xinmo Village landslide, the State Council, the Ministry of Land and Resources and various governmental departments at all levels in Sichuan Province immediately devoted their efforts into the emergency rescue operations, secondary hazard relief and geological surveying and monitoring. The preliminary results presented in this paper would not be achieved without a quick data acquisition, which has been facilitated greatly by the efforts of many staff members in different departments, to whom we express our sincere appreciation. We thank the Sichuan Provincial Surveying and Mapping Geographic Information Bureau, the High-resolution Earth Observation System Sichuan Data and Application Center, the Sichuan Shu Tong Geotechnical Engineering Company, the Beijing Digital Greenfield Technology Co. Ltd. and other units for the basic data collection. We express our gratitude to Prof. Yueping Yin from China Geological Environment Monitoring Institute, to Prof. Xiao Li from China Geological Survey, to Prof. Zhenhong Li from Newcastle University, to Prof. Lu Zhang and Prof. Mingsheng Liao from Wuhan University, to Prof. Qin Zhang from Chang'an University, to Prof. Shizhong Hong from Chengdu Earthquake Prevention and Hazard Mitigation Bureau, to Dr. Xinghui Huang from China Earthquake Networks Center to Prof. Yong Li from Chengdu University of Technology, to Prof. Chong Xu from Institute of Geology, China Earthquake Administration, for providing valuable information at the earliest time. We express sincere thanks to Dr. Yanan Jiang, Dr. Jing Ran, Xianxuan Xiao, Weiwei Zhan, Jing Ren, Yuanzhen Ju, Chen Guo, and other postgraduate students from Chengdu University of Technology for their hard work on the UAV aerial photography, GBSAR monitoring and other field work.

Funding This research is financially supported by National Science Fund for Distinguished Young Scholars of China (Grant No. 41225011), the Funds for Creative Research Groups of China (Grant No. 41521002), National Science Fund for Outstanding Young Scholars of China (Grant No. 41622206), the AXA Fund.

References

Allstadt K (2013) Extracting source characteristics and dynamics of the August 2010 Mount Meager landslide from broadband seismograms. J Geophys Res Earth Surf 118(3):1472–1490. https://doi.org/10.1002/jgrf.20110

Bromhead EN (2013) Reflections on the residual strength of clay soils, with special reference to bedding-controlled landslides. The Twelfth Glossop Lecture Q J Eng Geol Hydrogeol. https://doi.org/10.1144/qjegh2012-078

Chai HJ, Liu HC, Zhang ZY (1995) Landslide dams induced by Diexi earthquake in 1933 and its environmental effect. J Geol Hazards Environ Preserv 6(1):7–17 **(in Chinese)**

Chao WA et al (2017) A first near real-time seismology based landquake monitoring system. Sci Rep 7:43510. https://doi.org/10.1038/srep43510

Chen CH et al (2013) A seismological study of landquakes using a real-time broadband seismic network. Geophys J Int 194(2):885–898. https://doi.org/10.1093/gji/ggt121

Coe JA et al (2016) Rock-avalanche dynamics revealed by large-scale field mapping and seismic signals at a highly mobile avalanche in the West Salt Creek valley, western Colorado. Geosphere 12(2):607–631. https://doi.org/10.1130/GES01265.1

COMET (2014) (Center for Observation & Modelling earthquakes, volcanoes & Tectonic) (2017) Sentinel-1 satellites reveal pre-event movements and source areas of the Maoxian landslides, China[EB/OL]. http://comet.nerc.ac.uk/sentinel-1-satellites-reveal-pre-event-movements-source-areas-maoxian-landslides-china/?platform=hootsuite. 29 June 2017

Cruden DM, Varnes DJ (1996) Landslide types and processes. In: Turner AK, Schuster RL (eds) Landslides investigation and mitigation. Transportation research board, US National Research Council. Special Report 247, Washington, DC, (3)36–75

Deng B, Liu S, Liu S, Jansa L, Li Z, Zhong Y (2013) Progressive Indosinian N-S deformation of the Jiaochang structure in the Songpan-Ganzi Fold-Belt, Western China. PLoS One 8(10):e76732. https://doi.org/10.1371/journal.pone.0076732

Ekström G, Stark CP (2013) Simple scaling of catastrophic landslide dynamics. Science 339(6126):1416–1419. https://doi.org/10.1126/science.1232887

Fan X, Huang R (2013) The landslide story. Nat Geosci 6(5):325–326. https://doi.org/10.1038/ngeo1806

Huang R (2009) Some catastrophic landslides since the twentieth century in the southwest of China. Landslides 6(1):69–81. https://doi.org/10.1007/s10346-009-0142-y

Huang R, Li W (2009) Analysis of the geo-hazards triggered by the 12 May 2008 Wenchuan earthquake. China Bull Eng Geol Environ 68:363–371. https://doi.org/10.1007/s10064-009-0207-0

Huang R, Wang Z, Pei S, Wang Y (2009) Crustal ductile flow and its contribution to tectonic stress in Southwest China. Tectonophysics 473(3):476–489. https://doi.org/10.1016/j.tecto.2009.04.001

Hungr O, Leroueil S, Picarelli L (2014) The Varnes classification of landslide types, an update. Landslides 11(2):167–194. https://doi.org/10.1007/s10346-013-0436-y

Jones LM, Han WB, Hauksson E, Jin A, Zhang Y, Luo Z (1984) Focal mechanisms and aftershock locations of the Songpan earthquakes of August 1976 in Sichuan, China. J Geophys Res 89(9):7697–7708

Koi T, Hotta N, Ishigaki I et al (2008) Prolonged impact of earthquake-induced landslides on sediment yield in a mountain watershed: the Tanzawa region, Japan. Geomorphology 101:692–702. https://doi.org/10.1016/j.geomorph.2008.03.007

Korup O (2005) Large landslides and their effect on sediment flux in South Westland, New Zealand. Earth Surf Process Landf 30:305–323. https://doi.org/10.1002/esp.1143

Li SB, Lee SP (1954) On the application of seismic scales. Chin J Sin 3(01):35–54 (In Chinese with English abstract)

Li TC, Schuster RL, Wu JS (1986) Landslide dams in south-central China. In: Schuster RL (ed) Landslide dams-processes, risk, and mitigation: American Society of Civil Engineers Geotechnical Special Publication 3:146–162

Li C, Xu W, Wu J, Gao M (2016) Using new models to assess probabilistic seismic hazard of the North–South Seismic Zone in China. Nat Hazards 82(1):659–681. https://doi.org/10.1007/s11069-016-2212-5

Lin CH (2015) Insight into landslide kinematics from a broadband seismic network. Earth Planets Space 67(1):1–6. https://doi.org/10.1186/s40623-014-0177-8

Lin CH, Kumagai H, Ando M, Shin TC (2010) Detection of landslides and submarine slumps using broadband seismic networks. Geophys Res Lett 37:L22309. https://doi.org/10.1029/2010GL044685

Lin CH, Jan JC, Pu HC, Tu Y, Chen CC, Wu YM (2015) Landslide seismic magnitude. Earth Planet Sci Lett 429:122–127. https://doi.org/10.1016/j.epsl.2015.07.068

Ling S (2015) Landslide damming in Western Sichuan Province, China, with special reference to the 1786 Dadu River and 1933 Diexi events. M.Sc. Thesis, University of Waterloo, Ontario, Canada, 99 pp., https://uwspace.uwaterloo.ca/handle/10012/9496

Manconi A, Picozzi M, Coviello V, De Santis F, Elia L (2016) Real-time detection, location, and characterization of rockslides using broadband regional seismic networks. Geophys Res Lett 43:6960–6967. https://doi.org/10.1002/2016GL069572

Tang R, Wen D, Huang Z (1991) The quaternary activity characteristics of several major active faults in the Songpan Longmenshan region. Earthq Res China 7(3):64–71 (In Chinese)

Tang C, Zhu J, Li WL, Liang JT (2009) Rainfall-triggered debris flows following the Wenchuan earthquake. Bull Eng Geol Environ 68:187–194. https://doi.org/10.1007/s10064-009-0201-6

Tian B, et al. (2017) Mapping Thermokarst Lakes on the Qinghai–Tibet plateau using nonlocal active contours in Chinese GaoFen-2 multispectral imagery. IEEE Journal of selected topics in Applied Earth Observations and Remote Sensing. https://doi.org/10.1109/JSTARS.2017.2666787

TRE ALTAMIRA (2017) Data in Focus: Precursor of Maoxian Landslide Measured from Space[EB/OL]. http://tre-altamira.com/news/data-focus-precursor-maoxian-landslide-measured-space/. 2017–06-29

Wang LS, Yang LZ, Li TB, Xu XN, Wang XQ, Cui J (2008) Diexi earthquake-induced landslide, Min River, Sichuan Province (1933). In: Huang R, Xu Q (eds) Catastrophic landslides in China 57–93. Science Press, Beijing **ISBN: 9787030223500 (In Chinese)**

Wang Y, Huang R, Luo Y, Xu H (2011) The genetic mechanism of the Wenchuan earthquake. J Mt Sci 8(2):336–344. https://doi.org/10.1007/s11629-011-2096-5

Wei X, Chen N, Cheng W, He N, Deng M, Tanoli JI (2014) Long-term activity of earthquake-induced landslides: a case study from Qionghai Lake basin, Southwest of China. J Mt Sci 11(3):607–624. https://doi.org/10.1007/s11629-013-2970-4

Xu X, Wen X, Yu G, Chen G, Klinger Y, Hubbard J, Shaw J (2009) Coseismic reverse- and oblique-slip surface faulting generated by the 2008 Mw 7.9 Wenchuan earthquake, China. Geology 37(6):515–518. https://doi.org/10.1130/G25462A.1

Xu Q, Fan X, Huang R, Yin Y, Hou S, Dong X, Tang M (2010) A catastrophic rockslide-debris flow in Wulong, Chongqing, China in 2009: background, characterization, and causes. Landslides 7(1):75–87

Xu Q, Li WL, Dong XJ, Xiao XX, Fan XM, Pei XJ (2017) The Xinmocun landslide on June 24, 2017 in Diexi, Maoxian, Sichuan. characteristics and failure mechanism, 2017, Chinese Journal of Rock Mechanics and Engineering (accepted, In Chinese)

Yamada M, Matsushi Y, Chigira M, Mori J (2012) Seismic recordings of landslides caused by typhoon Talas (2011), Japan. Geophys Res Lett 39(39):342–343. https://doi.org/10.1029/2012GL052174

Yin Y, Cheng Y, Liang J, Wang W (2016) Heavy-rainfall-induced catastrophic rockslide-debris flow at Sanxicun, Dujiangyan, after the Wenchuan Ms 8.0 earthquake. Landslides 13(1):9–23. https://doi.org/10.1007/s10346-015-0554-9

Yu B, Wu Y, Chu S (2014) Preliminary study of the effect of earthquakes on the rainfall threshold of debris flows. Eng Geol 182(B):130–135. https://doi.org/10.1016/j.enggeo.2014.04.007

Zhang M, Yin Y (2013) Dynamics, mobility-controlling factors and transport mechanisms of rapid long-runout rock avalanches in China. Eng Geol 167(12):37–58. https://doi.org/10.1016/j.enggeo.2013.10.010

Zhang D, Wang G, Yang T, Zhang M, Chen S, Zhang F (2013) Satellite remote sensing-based detection of the deformation of a reservoir bank slope in Laxiwa Hydropower Station, China. Landslides 10(2):231–238. https://doi.org/10.1007/s10346-012-0378-9

X. Fan · Q. Xu (✉) · G. Scaringi · L. Dai · W. Li · X. Dong · X. Zhu · X. Pei · K. Dai
The State Key Laboratory of Geohazards Prevention and Geoenvironment Protection (SKLGP),
Chengdu University of Technology,
Chengdu, Sichuan 610059, China
Email: xuqiang_68@126.com

H.-B. Havenith
Department Géologie,
Université de Liège,
Liège, Belgium